Chemistry and electronic structure of AlInP (001) surfaces upon exposure to water and oxygen

M. A. Zare Pour[1,2,†], I. A. Ruiz Alvarado[3,†], J. Diederich[4,5,6,†], M. N. Qaisrani[7], S. Shekarabi[1], J. Koch[1], C. Höhn[4], C. Dreßler[7,8], D. Friedrich[4], W. Jaegermann[9], R. van de Krol[4,5], W. G. Schmidt[3], A. Paszuk[2], T. Hannappel[1,8,‡]

[1]Fundamentals of energy materials, Institute of Physics, Faculty of Mathematics and Natural Sciences, Technische Universität Ilmenau, 98693 Ilmenau, Germany
[2]BMFTR Junior Research Group PARASOL, Institute of Physics, Faculty of Mathematics and Natural Sciences, Technische Universität Ilmenau, 98693 Ilmenau, Germany
[3]Theoretical Materials Physics, Department of Physics, Universität Paderborn, 33095 Paderborn, Germany
[4]Institute for Solar Fuels, Helmholtz-Zentrum Berlin für Materialien und Energie GmbH, 14109 Berlin, Germany
[5]Institute of Chemistry, Technische Universität Berlin, 10623 Berlin, Germany
[6]Frick Chemistry Laboratory, Princeton University, NJ 08544 Princeton, United States of America
[7]Theoretical Solid State Physics, Institute of Physics, Faculty of Mathematics and Natural Sciences, Technische Universität Ilmenau, 98693 Ilmenau, Germany
[8]Institute of Micro- und Nanotechnologies, Technische Universität Ilmenau, 98693 Ilmenau, Germany
[9]Surface Science Laboratory, Department of Materials- and Geosciences, Technische Universität Darmstadt, Darmstadt 64287, Germany

[†]These authors contributed equally to this work.
[‡]Corresponding author: T. Hannappel, Email: thomas.hannappel@tu-ilmenau.de

List of Figures

List of Tables

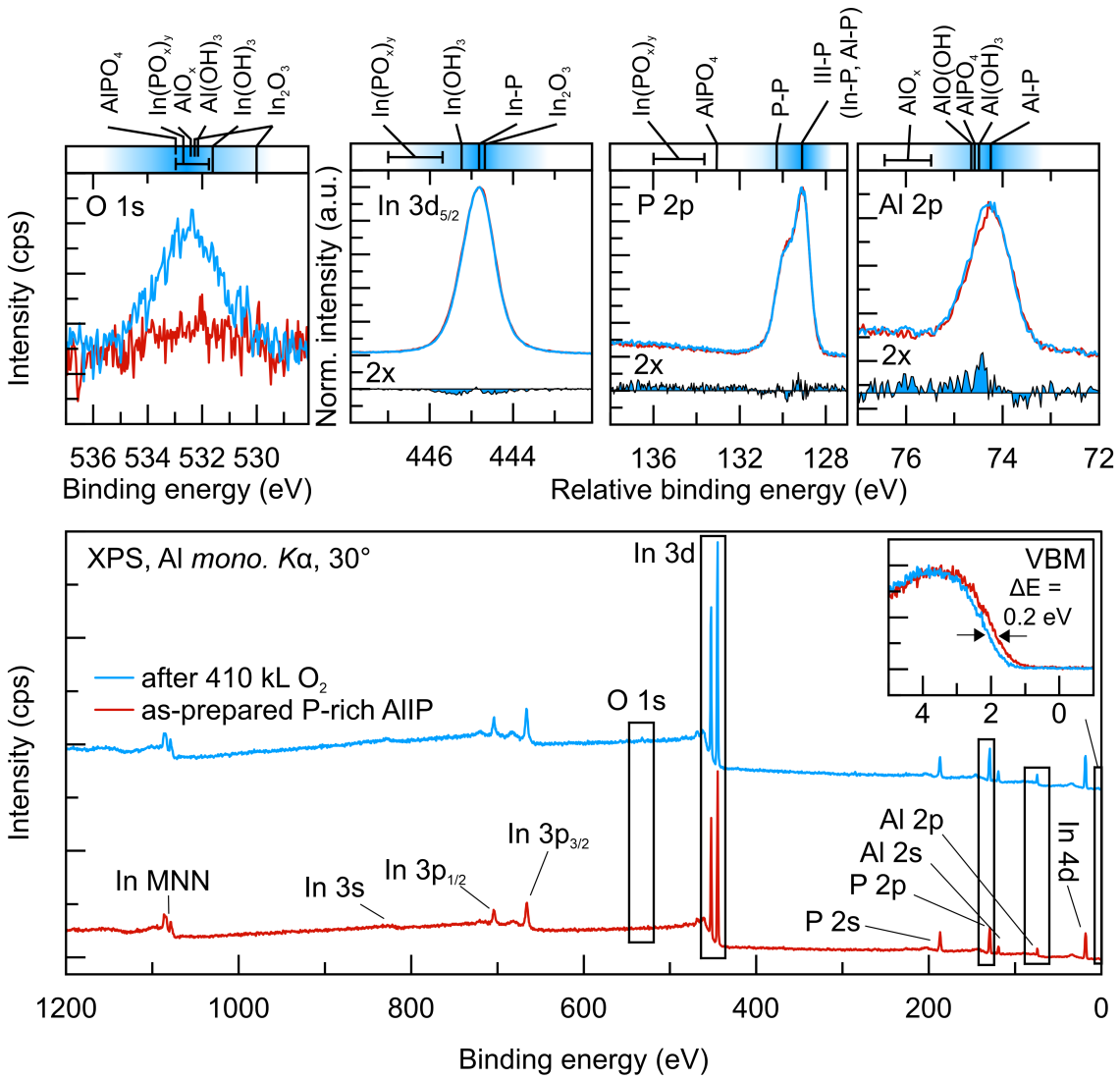

Figure S1: XP survey and HR spectra for P-rich AlInP (001), recorded before (red) and after exposure to 410 kL O_2 (blue). To demonstrate the spectral changes in In $3d_{5/2}$, P 2p, and Al 2p core levels induced by exposure, these spectra are normalized to their respective maximum intensity, and the post-exposure spectra are shifted to maximize overlap with the as-prepared spectra. Accordingly, the x-axis is labeled as "Relative binding energy." The horizontal bars positioned above each spectrum specify the BE ranges of various oxide species, serving as references to facilitate peak assignment. No C contamination was found upon O_2 exposure. Evolution of emission in the O 1s region is resolved; however, no significant changes are observed in the line shape of other core levels. This suggests limited interaction of O_2 molecules with the surface. However, subtle variations in the Al 2p line shape indicate potential interactions between Al atoms and O_2. Based on the emission lines, there is a potential for traces of Al−O−Al and Al−O−P to form. Validating the formation of Al−O−P presents is challenging due to the low sensitivity of the P 2p core level by X-ray photoemission spectroscopy (XPS); thus, the presence of a small amount is possible. The BE of O 1s may indicate that the surface reaction is governed by small amount of H_2O inside the exposure chamber.
However, the valence band maximum (VBM), along with all aluminium indium phosphide (AlInP) core levels, shifts approximately 200 meV towards higher binding energys (BEs), which can be associated with a partial reduction of surface states. This implies a reduction of the band bending (BB) towards the surface by 200 meV. This reduction can possibly be attributed to the elimination of surface P dangling bonds in the (2 × 2)-2D-1H surface structure. In a previous study [1] involving P-rich InP, it was demonstrated that the (2 × 2)-2D-1H surface structures, which pins the Fermi level by introducing P dangling bonds and creates midgap surface states, displays greater reactivity compared to the (2 × 2)-2D-2H surface. Consequently, these defects are expected to be more susceptible to chemical reactions during exposure experiments compared to other regions of the surface defined by the 2D-2H unit cell. Therefore, the reduction of surface states is likely due to the formation of Al−O−P bridges between P atoms in the first monolayer and Al atoms in the second monolayer. In these investigations, a key limitation is the resolution offered by laboratory-based XPS. Nevertheless, by comparing the results of water exposure with those from O_2 exposure, it becomes apparent that the P-rich AlInP surface reactivity to water is higher than to O_2. The most energetically favorable adsorption sites for both O_2 and H_2O are located between Al atoms in the sub-monolayers and between Al and P. Similarly, in each scenario, a partial reduction of the surface states are also observed.

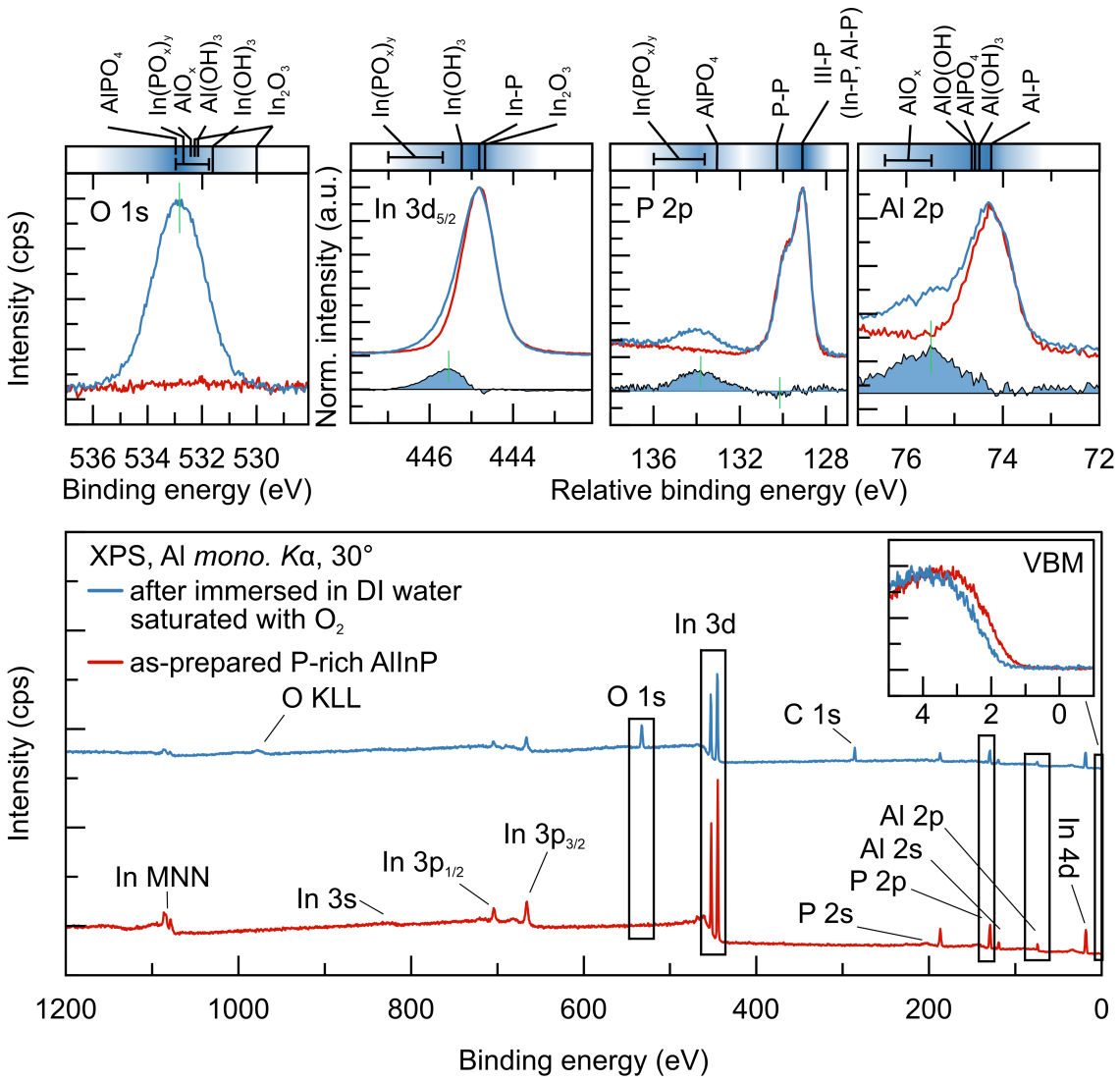

Figure S2: XP survey and HR spectra for P-rich AlInP (001), recorded before (red) and after immersing in DI water saturated with O_2 (blue). XPS measurements were done at 30° configuration. To demonstrate the spectral changes in In $3d_{5/2}$, P 2p, and Al 2p core levels induced by exposure, these spectra are normalized to their respective maximum intensity, and the post-exposure spectra are shifted to maximize overlap with the as-prepared spectra. Accordingly, the x-axis is labeled as "Relative binding energy." The horizontal bars positioned above each spectrum specify the BE ranges of various oxide species, serving as references to facilitate peak assignment.

Compared to water exposure in vacuum the emission line of O 1s is shifted to higher BE to 532.86 eV. Because also new emission in In $3d_{5/2}$ at 445.55 eV and P 2p at 133.96 eV core levels are evident, it indicates formation of higher concentration of $In-O-P$ ($In(PO_x)_y$) compared to in vacuum experiments. The emission of the P 2p line at approximately 130.10 eV is minimally diminished, suggesting that the $P-P$ dimers are only partially dissociated (highlighted by green line in the difference spectrum).

It is clear that the oxide contribution in Al 2p core level is greater than others meaning the surface is rich in Al oxide species. The peak maximum of the newly observed emission line in the Al 2p, located at 75.55 eV and highlighted by the green line, suggests that the principal Al-containing oxide specie are $Al-O-Al$ bonds. Compared to ultra-high vacuum (UHV)-based experiments, the rise in oxide concentration suggests the development of a thin oxide layer characterized by a more definite lattice structure, which is expected to exhibit higher stoichiometry. $Al-O-Al$ (AlO_x) and $In-O-P$ ($In(PO_x)_y$) emerge as the most dominant oxides on the surface. However, the exact stoichiometry of these species cannot be determined due to the limited resolution of the setup. Their electronic structure may significantly influence charge carrier separation.

The VBM and all core levels exhibit an energy shift of approximately 370 meV towards higher BEs, signifying that the surface states have undergone enhanced passivation due to contact with water/O_2, compared to lower exposure levels. Upon interaction with water/O_2, the VBM is observed at 1.62 eV, reflecting a reduction in the upward BB to 0.70 eV. This finding align with previous studies, in which InP, GaP, and gallium indium phosphide (GaInP) surfaces with oxide layers, both pre- and post-etching, were analyzed using photoemission spectroscopy (PES) measurements [2–4]. The study demonstrated that samples with a native oxide layer, as well as those chemically etched to remove such layers, exhibit Fermi level pinning, thereby inducing BB.

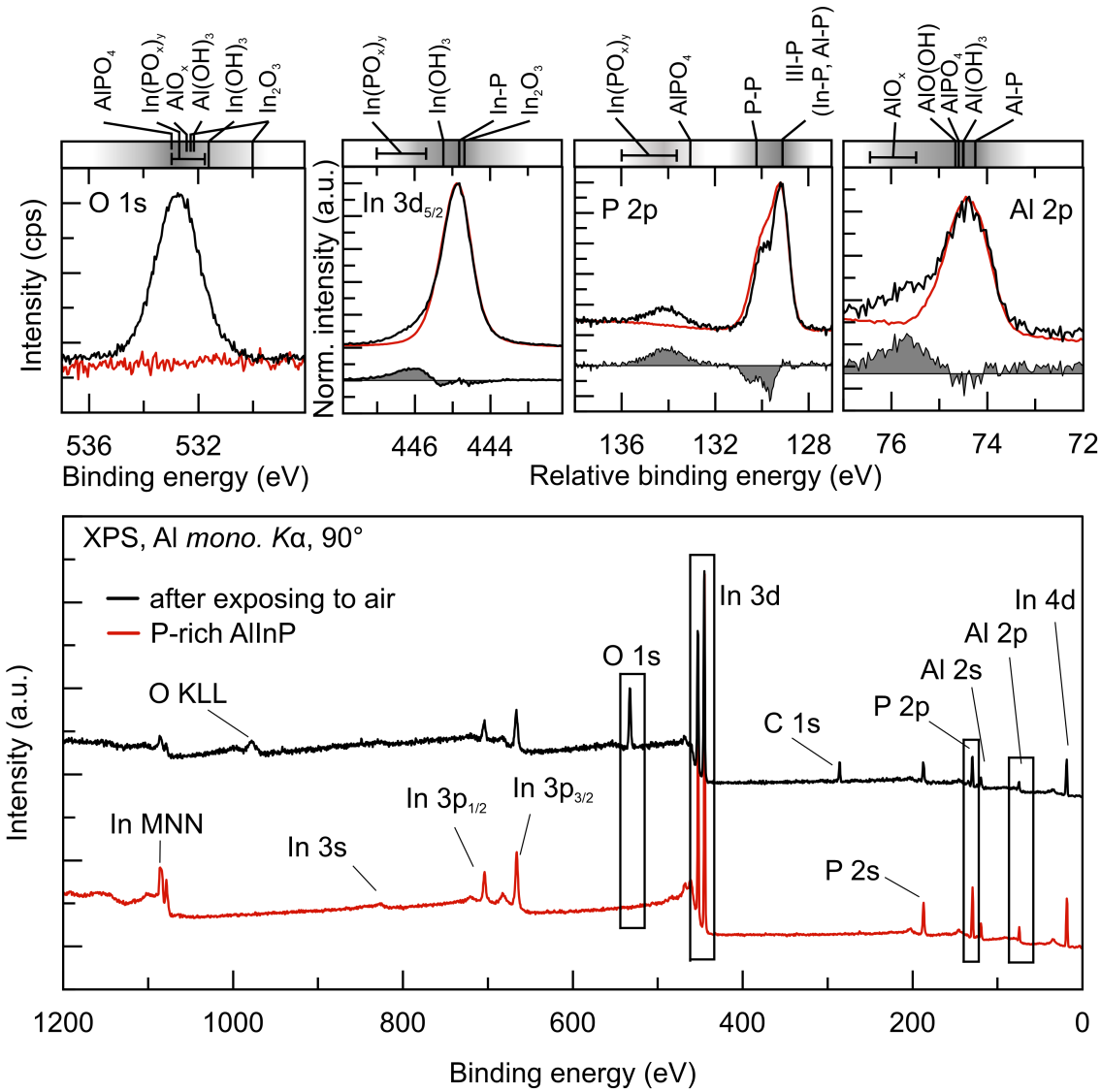

Figure S3: XP survey and HR spectra for P-rich AlInP (001), recorded before (red) and after exposure to air (black). In $3d_{5/2}$, P 2p, and Al 2p core levels are normalized to their respective maximum intensity, and the post-exposure spectra are shifted to maximize overlap with the as-prepared spectra. Accordingly, the x-axis is labeled as "Relative binding energy." Difference spectra vs P-rich are plotted. The horizontal bars positioned above each spectrum specify the binding energy ranges of various oxide species, serving as references to facilitate peak assignment.
Exposure of a P-rich AlInP surface to air leads to the formation of an oxide layer predominantly composed of the Al−O−Al and In−O−P. This is evidenced by the evolution of emission at 75.70 eV in Al 2p and at 446.00 eV in In $3d_{5/2}$, as indicated by the green guidelines. The dissociation of P−P dimers after air exposure is confirmed by the reduction in signal at approximately 129.90 eV, as revealed by the green guideline in the difference spectra.

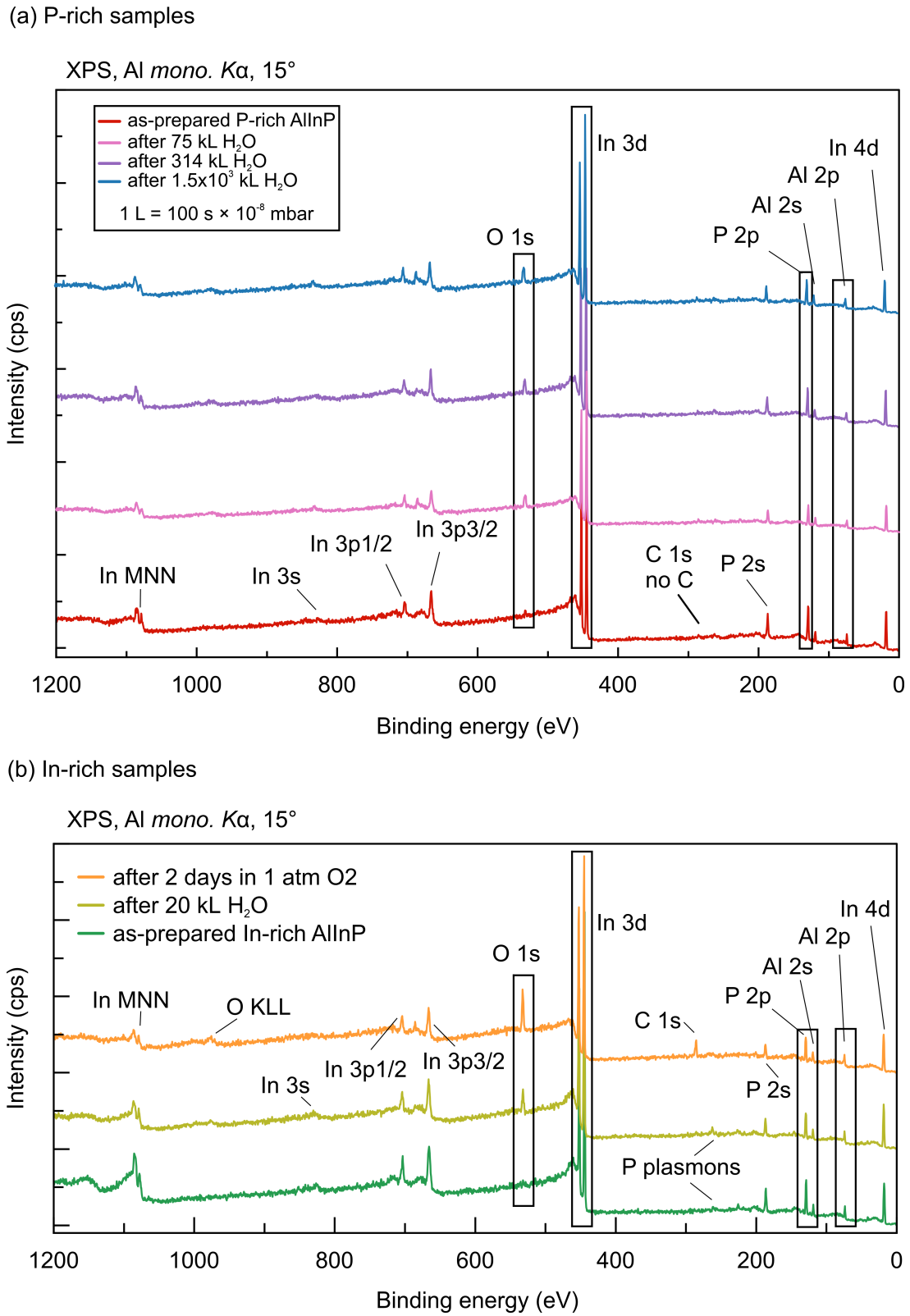

Figure S4: (a) XP survey for P-rich AlInP (001), recorded before (red) and after exposure to 75 kL (pink), 314 kL (purple), and after 1.5×10^3 kL (blue) of water. (b) XP survey for In-rich AlInP (001), recorded before (green) and after exposure to 20 kL of water (olive), and 2 days storing in 1 atm O_2 (yellow). No sign of C contamination of the as prepared samples was found.

Table S1: Binding energies (eV), FWHM (eV, in parenthesis if reported), E_g (eV) of for various oxide and hydroxides.

Compound	O 1s	In $3d_{5/2}$	P 2p	Al 2p	E_g	Ref.
In_2O_3	530.00 and 532.70 (1.80)	444.70			2.70-3.00	[5]
$In(OH)_3$	531.80 (2.40)	445.20 (1.50)			5.15	[4, 5]
InOOH	530.1	444.6			3.7	[6, 7]
$In(PO_x)_y$	531.80-533.00 (1.75-2.80)	445.70-447.0 (1.55-2.15)	133.90-136.00 (2.30)		4.50	[4, 5]
AlO_x	532.20			75.50-76.40	3.20-7.60	[8–11]
$Al(OH)_3$	532.10			74.40	5.27-5.54	[12, 13]
AlOOH	531.9			74.6	3.35-4.73	[14–17]
$AlPO_4$	533.00		133.10	74.40	5.90	[18–20]
P−OH	531.9 (2.5)		132.3 (2.3)			[21]

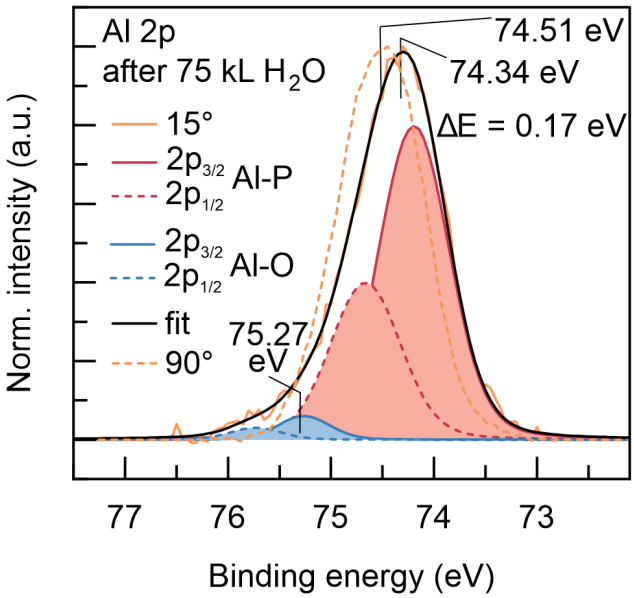

Figure S5: XP spectra of Al 2p core level at 90° and 15° measurements after the 75 kL water exposure. The fitting is shown only for XP spectrum of 15° measurement. The red and blue contributions are related to Al−P and Al−O bonds. The predominant spectral contribution arises from Al−P bonds (red). Additionally, a surface component with a $2p_{3/2}$ peak at 75.27 eV is detectable exclusively at 15°, attributed to Al−O bonds (blue). Notably, the XP spectra at 15° exhibit a shift of 170 meV towards higher BEs relative to the 90° measurement. A similar shift is also observable in the P 2p and In 3d core levels.

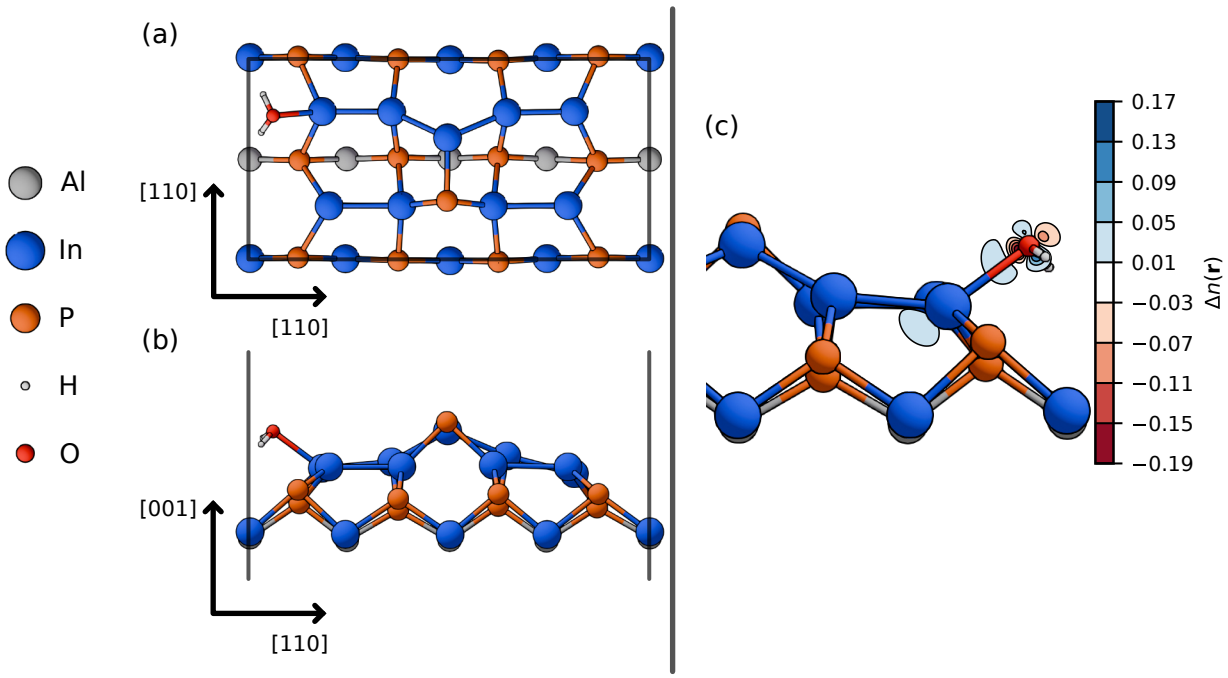

Figure S6: Top (a) and side (b) view of the most energetically favorable structural configuration for a single adsorbed water molecule at this site. Calculated water-induced charge redistribution for water adsorbed on the second row three-fold coordinated In atoms of the (2 × 4)-rInMD (c), Blue and red isosurfaces signify areas of charge accumulation and depletion, respectively.

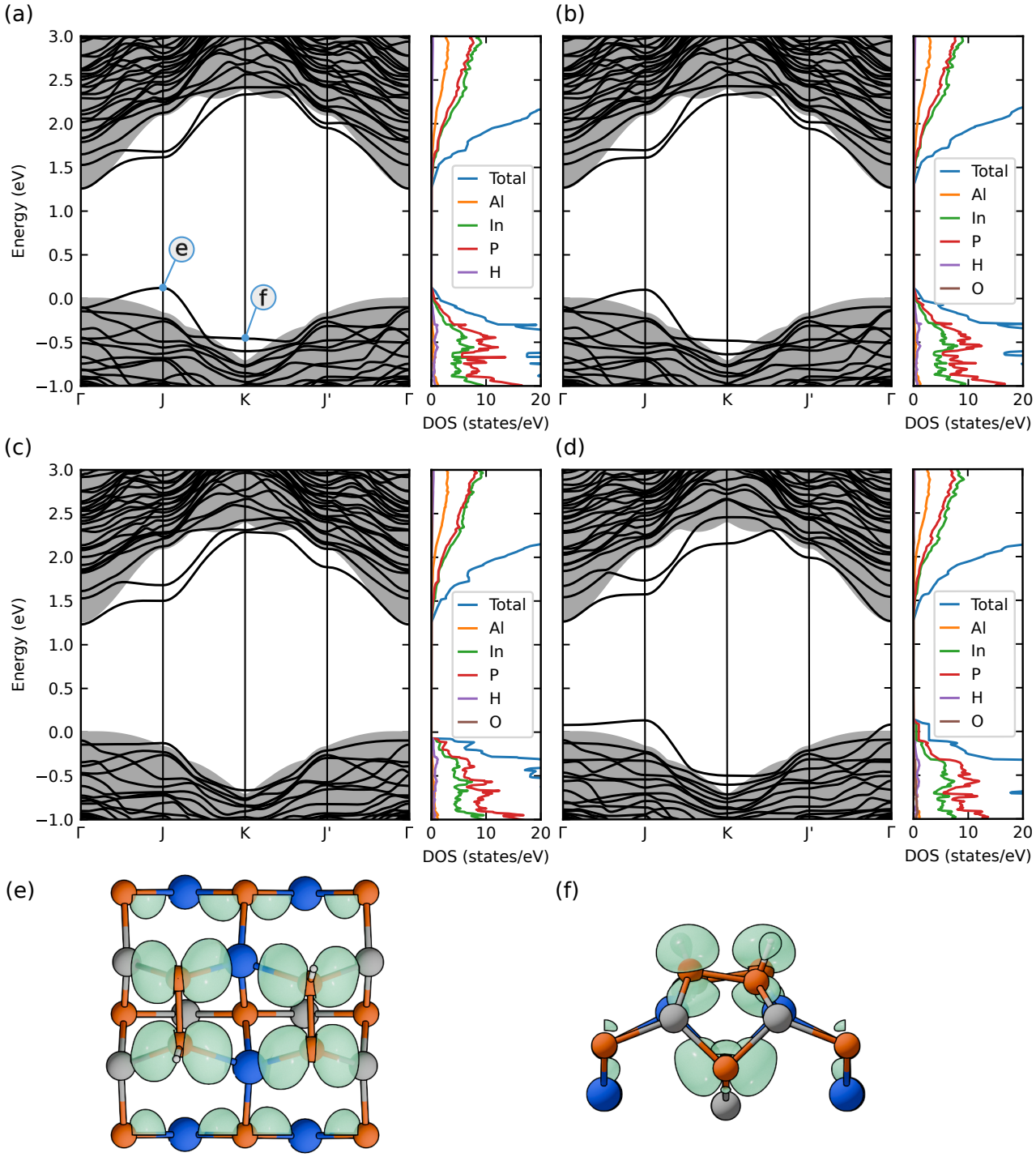

Figure S7: Band structure and the partially-decomposed density of states for the AlInP (2 × 2)-2D-2H clean surface (a), with an H_2O molecule adsorbed (b), an OH and H adsorbed (c) and an O atom adsorbed (d). The shaded areas indicate the projected bulk band structure. The orbital character of the highest occupied state of the (2 × 2)-2D-2H clean surface at the point J (e) and point K (f). The state at different k-points is indicated by the blue circles in (a). The adsorbed geometries are explained in the main text.

Note S1 Ab initio molecular dynamics investigation of P-rich and In-rich Water/AlInP Interfaces

As discussed in the main text, static DFT calculations at T = -273.15 °C (0 K) provided insight into the energetics and preferred adsorption geometries of single water and hydroxyl species on P-rich AlInP surfaces. However, it necessarily neglects thermal fluctuations, entropy, and dynamical hydrogen bonding–features essential to understanding realistic liquid–solid interfaces. To extend this understanding under more realistic interfacial conditions, we carried out finite-temperature Ab initio molecular dynamics (AIMD) simulations at 26.85 °C (300 K) for both P-rich and In-rich AlInP (001) surfaces interfaced with explicit water. These simulations thus serve to extend and contextualize the T = -273.15 °C (0 K) picture, revealing how interfacial structure, dipole alignment, and reactivity signatures unfold in the presence of an explicit solvent environment.

Figure S8 (b) and S8 (d) present a quantitative comparison of the time-averaged interfacial water structure for the P-rich and In-rich surfaces, respectively. Shown are normalized atomic density profiles for surface and water atoms along the surface normal z, as well as the orientational distribution of water molecules, measured by the ensemble average $\langle \cos\theta(z) \rangle$. Here, θ is the angle between the water dipole vector (defined from the oxygen atom to the midpoint of the two hydrogen atoms) and the surface normal. Positive values of $\langle \cos\theta \rangle$ indicate O-down orientation (oxygen toward the surface), while negative values indicate H-down orientation (hydrogens toward the surface). While a more rigorous dipole estimate can be obtained from electronic structure via Wannier centers, the geometric definition employed here provides a consistent and physically intuitive approximation of the dipole orientation as a function of depth.

For the P-rich surface (Figure S8 (b)), the water structure remains largely molecular and non-dissociative. A pronounced positive peak in $\langle \cos\theta \rangle$ (approximately +0.7) is observed at the first hydration layer near $z \sim 20$ Å, indicating a strong preference for O-down orientation. The corresponding density profiles show mostly the water molecules confined above the terminal hydrogen atoms on the surface, with very few interact weekly with subsurface Al or In atoms in the trench regions between P−P dimers as illustrated in the representative snapshot shown in Figure S8b. This structured, ordered first layer supports the formation of a transient dipole upon initial water contact, as observed experimentally through shifts in photoemission cutoffs. The absence of spontaneous dissociation during the 20 ps simulation is consistent with the chemical inertness of P−P dimers and the experimentally observed low reactivity of this termination toward water.

For the In-rich surface, the behavior of interfacial water differs markedly from that observed on the P-rich termination. The first hydration layer forms much closer to the surface, with water molecules making direct contact with undercoordinated surface In atoms. This is reflected in the density profile, which shows a sharp peak at lower z values compared to the P-rich case, and in the orientational profile $\langle \cos\theta(z) \rangle$, which exhibits a shallow negative dip (around −0.1) near the surface. This partial H-down orientation suggests stronger hydrogen bonding interactions between water molecules and the exposed In atoms, potentially preconditioning water for proton transfer. A representative AIMD snapshot (Figure S8 (c)) illustrates this configuration, showing a water molecule interacting simultaneously with surface and sub-surface In atoms. Beyond this H-down layer, a strong positive peak in $\langle \cos\theta(z) \rangle$ is observed, indicating that the second hydration layer adopts an O-down orientation consistent with bulk-like water structuring and electrostatic layering effects. The radial distribution functions (RDFs) further support this picture (see the discussion below), with pronounced O_w–In coordination peaks suggesting stronger water-In interactions on this surface. These observations align with experimental photoemission data showing a higher degree of hydroxylation and oxide formation on In-rich surfaces. While direct dissociation events are not observed within the 20 ps AIMD timescale, the observed proximity of water to surface In atoms and the orientational bias together indicate a more reactive interfacial environment, one that may facilitate proton transfer and hydroxylation over longer timescales.

To further quantify the nature of interfacial water–surface interactions, we computed the distribution of pair distances between water oxygen atoms and surface atoms (Al, In, P) during the AIMD trajectories. Specifically, we consider oxygen–surface atom pair counts within a 3.5 Å cutoff, a typical coordination shell radius for identifying hydrogen bonding and weak chemisorption—and construct radial distribution functions (RDFs) averaged over time. These allow us to assess the degree of water coordination with different surface elements and identify specific bonding motifs that may not be apparent from density profiles alone.

Figure S9 presents these pair count distributions for both surface terminations. In the P-rich case, a clear peak in the In$-O_w$ distribution is observed just beyond 2.0 Å (Figure S9a), indicating direct interaction of water oxygen atoms with In sites in trench region. A broader peak for Al appears around 3.5 Å, suggesting weaker or more distant interaction. Interestingly, the P$-O_w$ distribution also shows a peak, reflecting lateral proximity of water to the terminal P atoms, though not direct bonding. Overall, the coordination number (Figure S9c) is highest for P, followed by In and then Al. These trends help reconcile the apparently inert P-rich surface with the subtle dipole changes observed experimentally, and highlight the role of surface morphology (e.g., trenches)

in mediating water access to subsurface atoms.

In contrast, the In-rich surface shows markedly stronger and more structured water–metal interactions. The In$-$O$_w$ distribution (Figure S9b) features a dominant peak below 2.2 Å, indicating robust coordination of water oxygen atoms to surface In sites. Beyond this, secondary peaks reflect longer-range structuring, suggesting an extended solvation environment with multiple layers of water interacting with In atoms. Coordination with Al atoms is negligible in this case, consistent with Al being more buried. The P$-$O$_w$ RDF, however, still shows a noticeable feature, though at a longer distance, suggesting interaction between water and exposed P atoms, likely through hydrogen bonding rather than direct O$-$P coordination.

Taken together, the pair distributions emphasize the contrast in reactivity and solvation environments at the two terminations. While the P-rich surface exhibits more restrained, trench-limited interactions, the In-rich surface promotes strong water binding and structural ordering near the surface—behavior consistent with experimental observations of rapid hydroxylation and oxide formation on In-rich AlInP. Importantly, these coordination signatures are beyond to be captured in the T = -273.15 °C (0 K) calculations, where adsorption was limited to isolated molecules. The AIMD results thus reveal dynamic, cooperative effects that emerge only under thermal and solvent conditions.

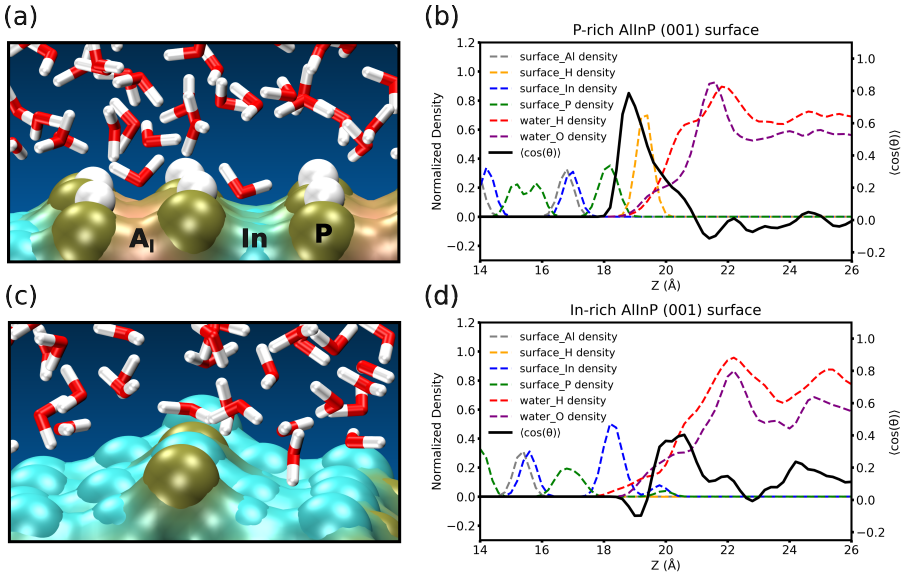

Figure S8: Representative snapshots and structural analysis from AIMD simulations illustrating water–surface interactions for both surface terminations. Panels (a) and (c) show side views of the P-rich and In-rich AlInP (001) surfaces, respectively, with interfacial water. Surface atoms are color-coded as indicated in panel (a). A van der Waals representation, combined with an isosurface highlight, illustrates trench regions on the surfaces for visual clarity. Panels (b) and (d) present the spatial distribution and orientational ordering of interfacial water near the P-rich and In-rich surfaces, respectively. Dashed curves show normalized one-dimensional number density profiles of surface atoms (Al, In, P, and surface-bound H) and water molecules (O and H) along the surface normal (z-axis). The solid black line represents the average dipole orientation of water molecules, expressed as $\langle \cos\theta(z) \rangle$, where θ is the angle between the water dipole vector (from O to the midpoint of H atoms) and the surface normal. Positive values indicate O-down orientation toward the surface, while negative values correspond to H-down configurations.

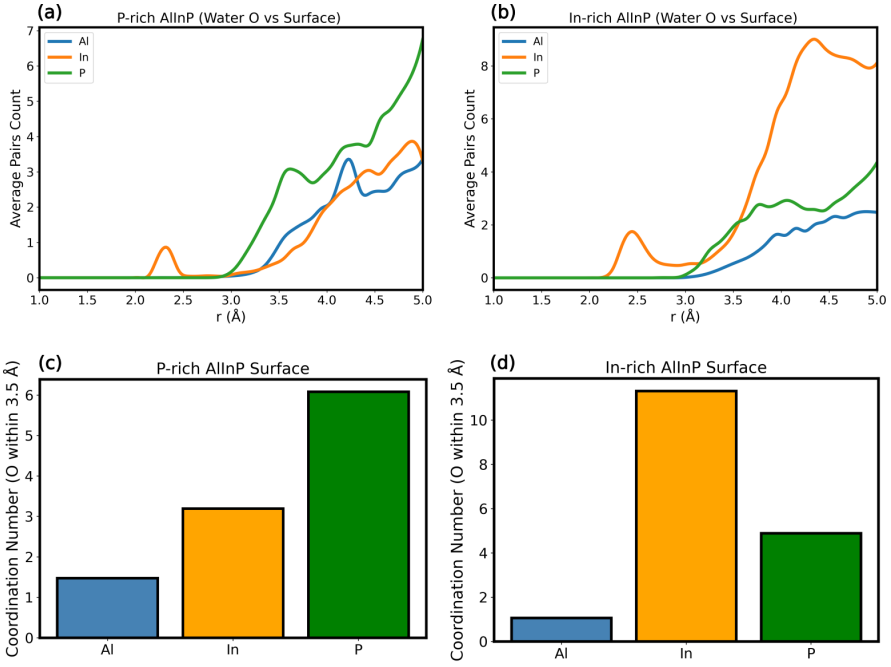

Figure S9: Radial distribution functions (RDFs) and coordination analysis of interfacial water with surface atoms from AIMD simulations. The un-normalised pair count distribution functions are computed between water oxygen atoms (O_w) and surface atoms (Al, In, P), averaged over the equilibrated trajectories for (a) P-rich and (b) In-rich AlInP (001) surfaces. (c) and (d) corresponds to the coordination number up to a cutoff of 3.5 Å , providing a quantitative measure of local water–surface interactions. For the P-rich surface, water oxygen atoms preferentially coordinate with subsurface In atoms via trench penetration, while P and Al exhibit weaker or more distal interaction. In contrast, the In-rich surface shows strong, short-range coordination with exposed In atoms and more structured solvation layers, consistent with enhanced water reactivity. These distributions highlight termination-dependent hydration structure and bonding motifs not accessible from static calculations alone.

Note S1.1 Computational Details for AIMD simulations

To investigate the structure and dynamics of the AlInP (001)/H_2O interface under realistic conditions, we performed ab initio molecular dynamics (AIMD) simulations using the open-source CP2K package.[22–24] The starting configurations for these simulations were constructed by solvating the optimized surface geometries obtained from our T = -273.15 °C (0 K) DFT calculations with explicit water molecules. Prior to the AIMD runs, the solvated systems were relaxed using the BFGS optimization algorithm to remove residual forces and adjust interfacial hydrogen bonding.

All AIMD simulations were carried out within the Born–Oppenheimer approximation, where the nuclei are propagated classically, and the electronic structure is evaluated on-the-fly using density functional theory. We employed the PBE exchange–correlation functional,[25, 26] along with dual Gaussian and plane-wave basis sets of DZVP-MOLOPT-SR-GTH type,[27] and norm-conserving GTH pseudopotentials.[28, 29] Long-range van der Waals interactions were accounted for using the empirical D3 dispersion correction by Grimme.[30]

The simulations were performed in the canonical (NVT) ensemble at a target temperature of 76.85 °C (350 K), regulated by a Nosé–Hoover chain thermostat.[31–33] This slightly elevated temperature was chosen to partially compensate for the known over-structuring of water with the PBE functional, and to accelerate interfacial sampling on accessible simulation timescales.[34]

We modeled two distinct surface terminations: (i) a P-rich AlInP (001)-water interface and (ii) an indium-rich water/AlInP (001) interface. The P-rich model comprised 100 water molecules (564 total atoms), while the In-rich model included 177 water molecules (775 total atoms). Each system was equilibrated and propagated for a total duration of 20 ps. Due to the larger number of atoms in the In-rich system, the simulation throughput was limited to approximately 450 AIMD steps per day (corresponding to 250 fs), which translates to roughly 5 days of computational time per picosecond of trajectory. Despite these constraints, we were able to obtain meaningful sampling of structural and orientational properties at the interface.

Table S2: Peak maximum position of core levels and VBM before and after 1.5×10^3 kL H_2O exposure.

Core levels	**Peak maximum position (eV)**			
	as-prepared P-rich		**after 1.5×10^3 kL H_2O**	
	90°	**15°**	**90°**	**15°**
Al 2p	74.42	74.20	74.60	74.46
P 2p	129.22	129.15	129.43	129.30
In $3d_{5/2}$	444.90	444.80	445.10	445.02
O 1s	—	—	532.45	532.61
VBM	1.40	1.12	1.60	1.36

Note S2 Band diagram

We drew the energetic band alignment of P- and In-rich AlInP based on doping concentration and XPS and UPS results as we already discussed in Ref.[35]. The Fermi level position in the bulk material is calculated by using the **equation S1**,

$$E_{CBM} - E_F = k_B T \ln \frac{N_C}{n_D} = 6meV \tag{S1}$$

where n_D is the doping concentration of the AlInP layer (2×10^{18} cm^{-3}, Si as a donor dopant), $k_B T$ is the Boltzmann term, and N_C is the AlInP's effective CB DOS, which is taken as the average of the AlP and InP DOS [36]. According to this calculation, the bulk Fermi level is approximately 6 meV below the CBM in both samples. Through XPS and UPS measurements, the VBM of the P-rich AlInP surface before exposure is determined to be 1.30 eV below the Fermi level, as shown in Figure 2 (b) and the VBM of the In-rich AlInP surface before exposure is determined to be 0.50 eV below the Fermi level, as shown in Figure 10 (b). This indicates the presence of surface states near the mid-gap position, given an AlInP band gap of 2.3 eV [37], as we discussed in Ref. [35]. The difference between the measured (by XPS/UPS on the surface) and calculated positions of the Fermi level relative to the VB in the bulk suggests a significant BB toward the surface, with a value of $BB_{\text{P-rich}} = 1.0$ eV and $BB_{\text{In-rich}} = 1.8$ eV. This phenomenon is due to the presence of surface states with electron displacement to the surface, hence pinning the Fermi level. These are illustrated in Figure 4 (a) and Figure 12 (a) for P-rich and In-rich AlInP before exposure, respectively.

Upon exposure, the changes are anticipated to be limited to the surface of AlInP, leaving the bulk unaffected. Thus, the band alignment within the bulk of P- and In-rich AlInP remains stable, meaning Fermi level is still 6 meV below the CBM in the bulk. However, alterations occur in the VBM of the surfaces. Analysis of UPS results allows the distinction of two edges: those of the oxides/hydroxides and the underlying AlInP. For the P-rich sample, the VBM of AlInP increases to 1.45 eV below the Fermi level after 314 kL and stabilizes with further exposure (see Figure 2 (b)). This results in a reduction in BB from 1.00 eV (bare surface) to 0.85 eV (after exposure). Meanwhile, the VBM of the surface oxides/hydroxides shifts from 3.70 eV after 314 kL to 4.05 eV following 1.5×10^3 kL of water exposure. The VBO between AlInP and oxides/hydroxides is calculated based on their VB edge difference, resulting in a VBO of 2.25 eV after 314 kL and 2.60 eV after 1.5×10^3 kL of water exposure. Accordingly the band alignment after exposure experiments are depicted in Figure 4 (b,c).

For In-rich AlInP, the band alignment can similarly be determined. During exposure experiments, the VB edge of oxides/hydroxides appears in the UPS data, as depicted in Figure 10 (c). After a 20 kL water exposure, the VBM of oxides/hydroxides is at 3.30 eV, whereas prolonged exposure to O_2 results in a VBM of 3.80 eV. Notably, the VB edge of AlInP beneath the oxides/hydroxides remains at 1.45 eV, as shown in Figure 10 (b,c). Consequently, the BB in AlInP is 1.85 eV, similar to P-rich sample. The VBO is 1.85 eV following a 20 kL water exposure, increasing to 2.35 eV after extended O_2 exposure experiments.

Table S3: Atomic concentrations (%) of P-rich AlInP exposed to varying water dosages, based on 90° XPS measurements.

Sample	**Atomic concentrations (%)**			
	Al	**In**	**P**	**O**
P-rich	24.3	25.5	50.2	0.0
after 75 kL	24.0	24.8	47.2	3.9
after 314 kL	23.2	22.5	47.9	6.4
after 1.5$\times 10^3$ kL	23.4	22.6	46.6	7.4

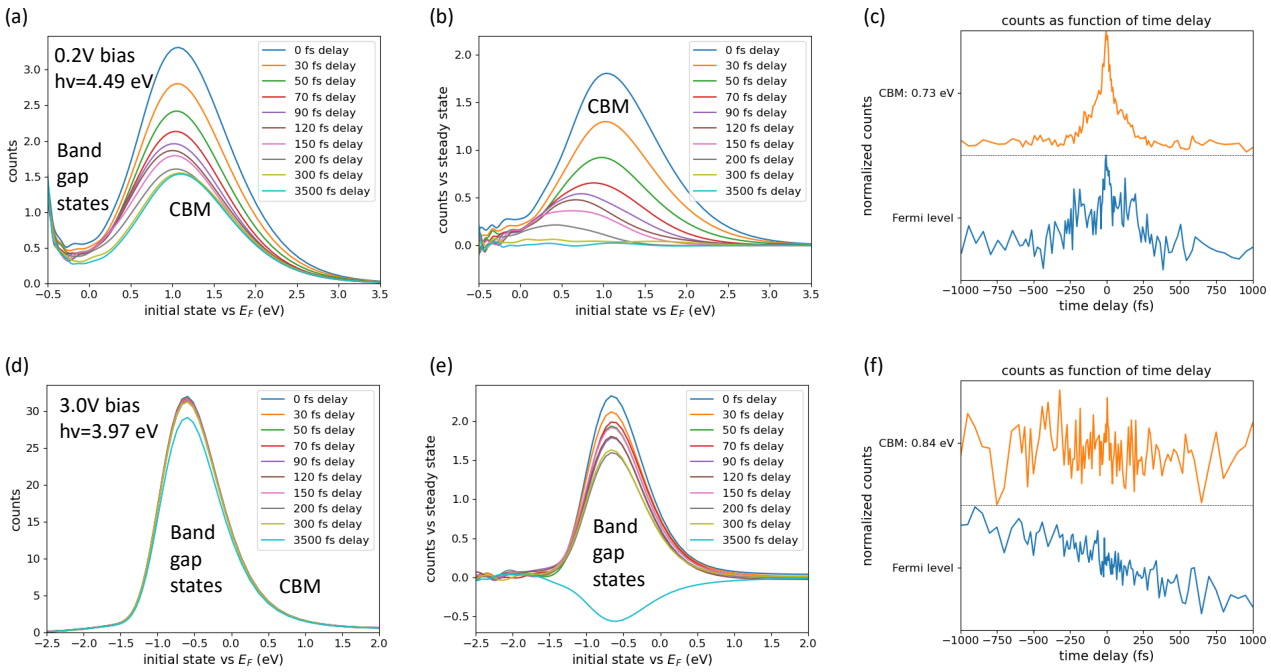

Figure S10: Tr-2PPE data for the bare P-rich AlInP surface using 0.2V bias at pump and probe photon energies hv=4.49 eV in (a, b, c) and 3.0V bias at hv=3.97 eV for (d, e, f). In the latter, there is some drift in emission with delay time, likely due to a small misalignment between pump and probe. The larger applied bias starts to disturb surface features, whilst the lower 0.2V bias allows for observations of CBM features especially. The emission cut-off appears to not be affected significantly by bias, indicating it is a surface feature. At 0.2V bias, no cut-off is observed, showing that it is not related to detector limits. The cut-off (corrected for the reduced photon energy of 3.97 vs 4.49 eV) does not move at 3.0V bias, indicating it is indeed related to surface properties rather than to detector- or other set-up related properties.

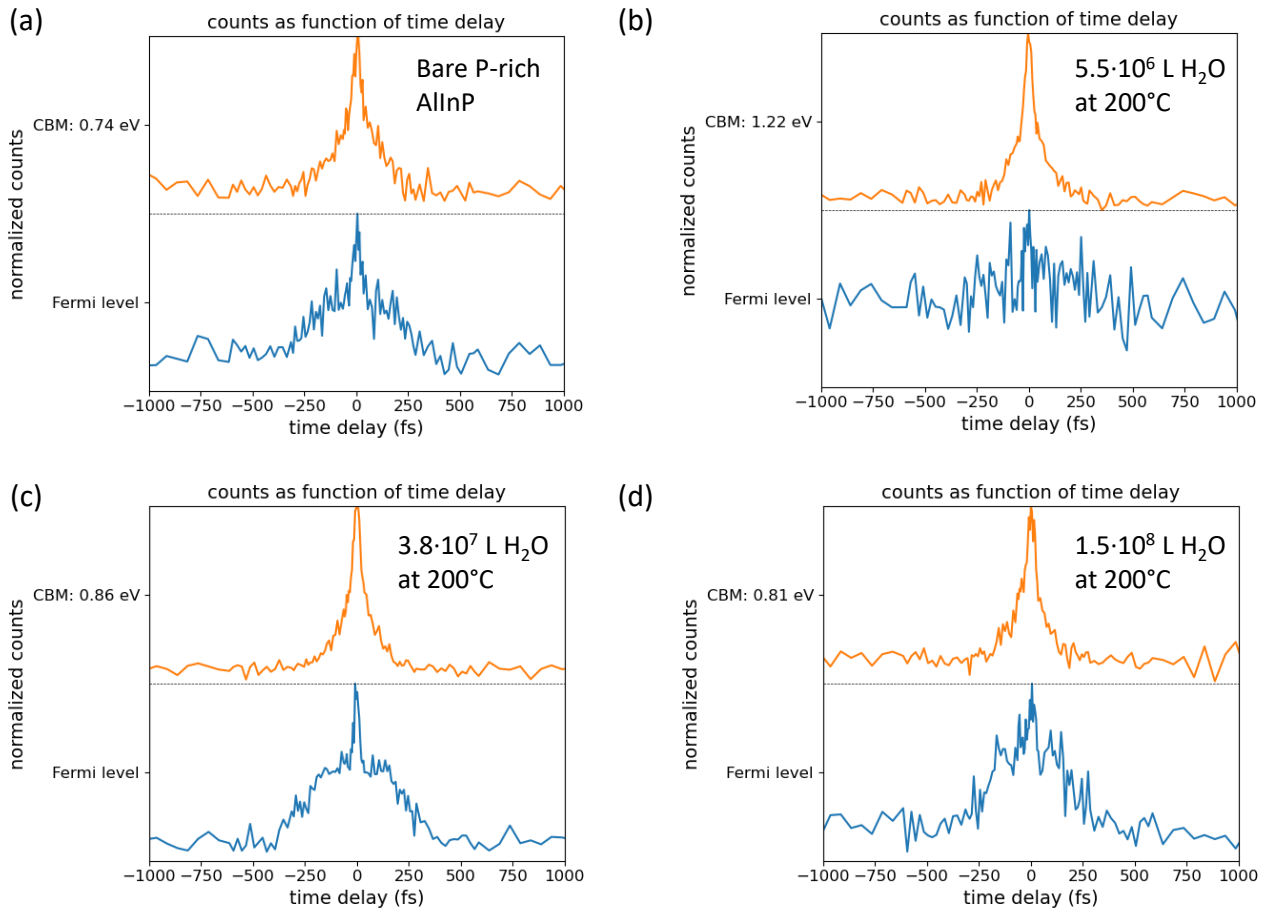

Figure S11: The time-dependence of emission at the CBM and Fermi level are plotted for the bare P-rich AlInP surface (a), and after 5.5×10^6 L (b), 3.8×10^7 L (c), and 1.5×10^8 L (d) water exposure at sample temperatures of 200 °C. CBM emission remains largely unchanged, whilst time-dependent emission from around the Fermi level decreases after initial 5.5×10^6 L water exposure and cannot be clearly separated from the noise, but again increases afterwards, as also observed in Figure 7. As previously discussed, UPS shows the DOS of mid-gap states decreasing with water exposure, which should be correlated with decreased emission in tr-2PPE, as we observe for initial water exposure. At high exposure levels, the emission cut-off shifts to lower kinetic energies, revealing more of the mid-gap emission peak and reuslting in increased emission despite the reduced DOS.

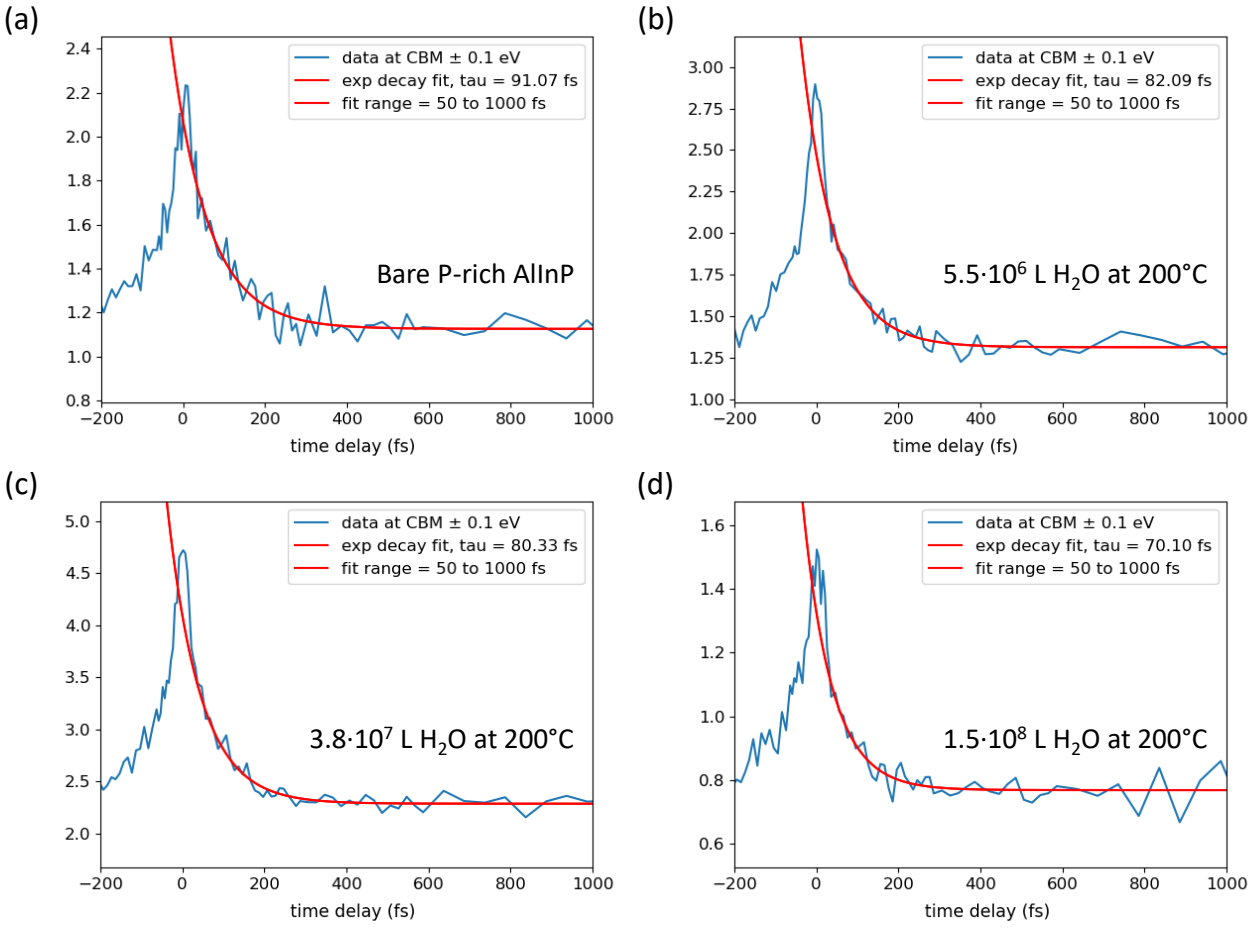

Figure S12: Decay times for emission from the CBM the bare P-rich AlInP surface (a), and after 5.5×10^6 L (b), 3.8×10^7 L (c), and 1.5×10^8 L (d) water exposure at sample temperatures of 200 °C. Assuming an exponential decay, decay times do not change significantly between exposure levels, starting at around 90 fs, with only a 10 fs drop after initial water exposure, and another 10 fs drop with further exposure. This reduction in CBM lifetime is likely related to added scattering/relaxation pathways in the nascent oxide, introducing defect states or phonons unrelated to the mid-gap states pinning the Fermi level.

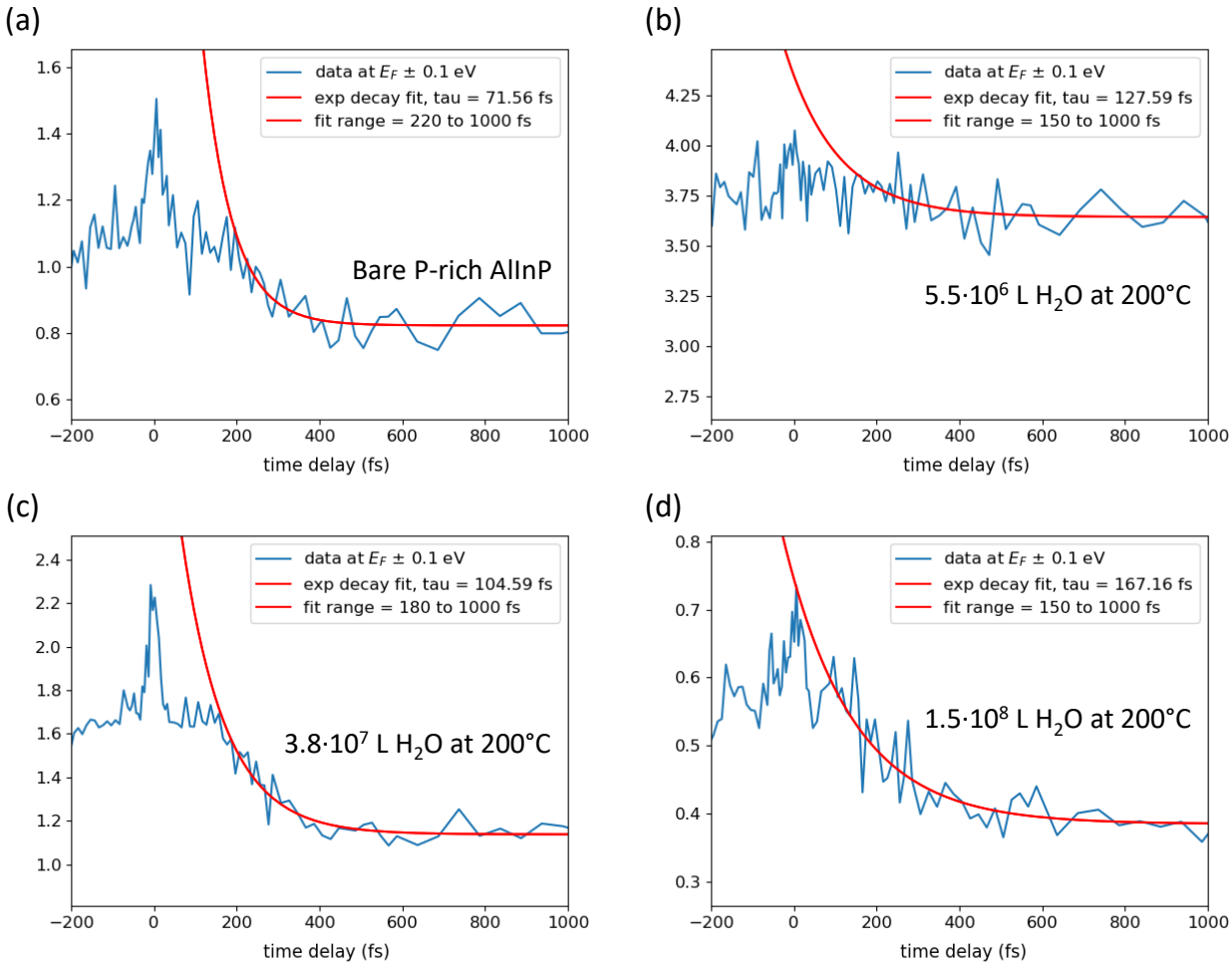

Figure S13: Decay times at the CBM are shown, again for the bare P-rich AlInP surface (a), and after 5.5×10^6 L (b), 3.8×10^7 L (c), and 1.5×10^8 L (d) water exposure at sample temperatures of 200 °C. Lifetimes increase by more than a factor of 2 with water exposure, whilst peak occupancy is reached around the same time at each exposure level. The latter is likely due to CBM lifetimes being unaffected by exposure, so electrons reach the Fermi level at similar times. Decay from mid-gap states is slowed, indicating some decay channels are suppressed by water exposure and the resulting surface oxidation. This agrees with previous results on P-rich InP, in which some surface state decay times were slowed by water physisorption and P-oxide formation, in part through damping of surface phonon modes.

Table S4: For each water exposure step, the positions of the emission cut-off at 1.0 V sample bias are given, as well as the position of the low-energy emission peak and CBM position, CBM and Fermi level lifetimes, as well as UPS work functions, VBM position relative to Fermi level and the expected CBM position based on the UPS results. The latter deviates from tr-2PPE results by +0.35 and -0.37 eV on the bare P-rich AlInP surface and after 5 pulses of water exposure respectively, likely related to surface dipole moments due to P−P dimers and adsorbed OH^- groups after initial water exposure. Data is taken from Figure 6, 7, S10, S11, S12, and S13.

Water exposure level	**Cut-off vs vacuum (eV)**	**Cut-off vs min. energy range (eV)**	**Low-energy peak vs vacuum (eV)**	**CBM emission vs E_f (eV)**	**CBM decay const. (fs)**	**E_f max occupancy (fs)**	**Fermi level decay time (fs)**	**UPS Φ (eV)**	**VBM vs E_f (eV)**	**VBM vs vacuum (eV)**	**CBM vs vacuum (VBM + 2.3 eV) (eV)**	**Expected CBM emission vs E_f (eV)**
Bare	-0.56	0.44	-0.44	0.74	91 ± 10	131 ± 20	72 ± 20	4.18	-1.21	-5.39	-3.09	1.09
5 hc	-0.38	0.62	-0.25	1.22	82 ± 10	unknown	unknown	4.50	-1.45	-5.95	-3.65	0.85
35 hc	-0.69	0.31	-0.60	0.87	80 ± 10	136 ± 20	105 ± 20	4.16	-1.41	-5.57	-3.27	0.89
135 hc	-0.70	0.30	-0.59	0.82	70 ± 10	125 ± 20	167 ± 40	4.14	-1.43	-5.57	-3.27	0.87

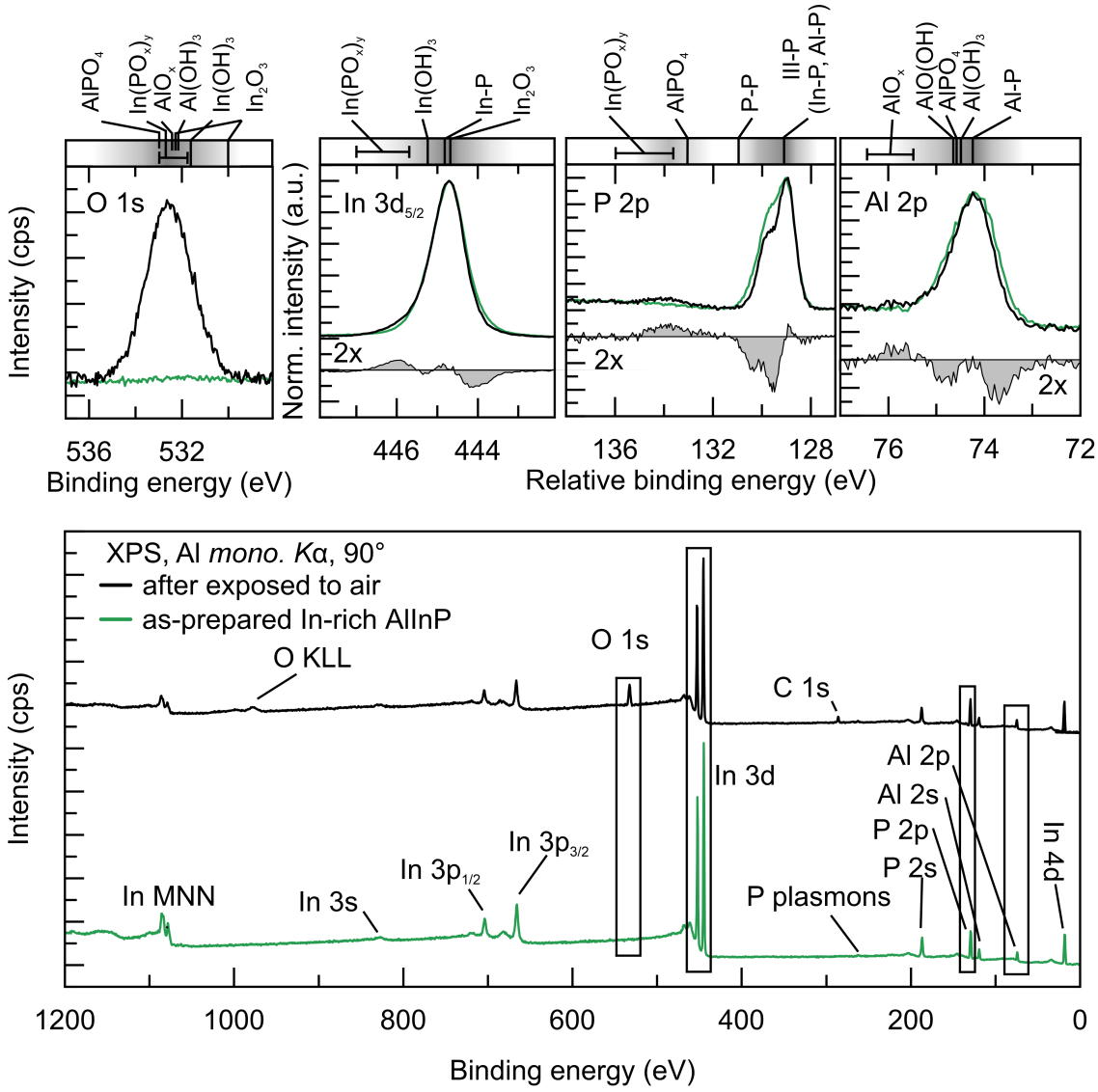

Figure S14: XP survey and HR spectra for In-rich AlInP (001), recorded before (green) and after exposure air (black). In $3d_{5/2}$, P 2p, and Al 2p core levels are normalized to their respective maximum intensity, and the post-exposure spectra are shifted to maximize overlap with the as-prepared spectra. Accordingly, the x-axis is labeled as "Relative binding energy." Difference spectra vs In-rich are multiplied to two and plotted. The horizontal bars positioned above each spectrum specify the binding energy ranges of various oxide species, serving as references to facilitate peak assignment.
Exposure of an In-rich AlInP surface to air results in the formation of an oxide layer primarily consisting of the In−O−P, rather than other types of oxides. The reduction in signal at 444.05 eV suggests the dissociation of In−In dimers, a process we have also observed to occur with low water dosage due to their high reactivity. Furthermore, the emission at 129.90 eV decreases, implying that the remaining P−P dimers from preparation dissociate upon air exposure. Surprisingly, the Al 2p core level does not exhibit any new emissions from oxide species.

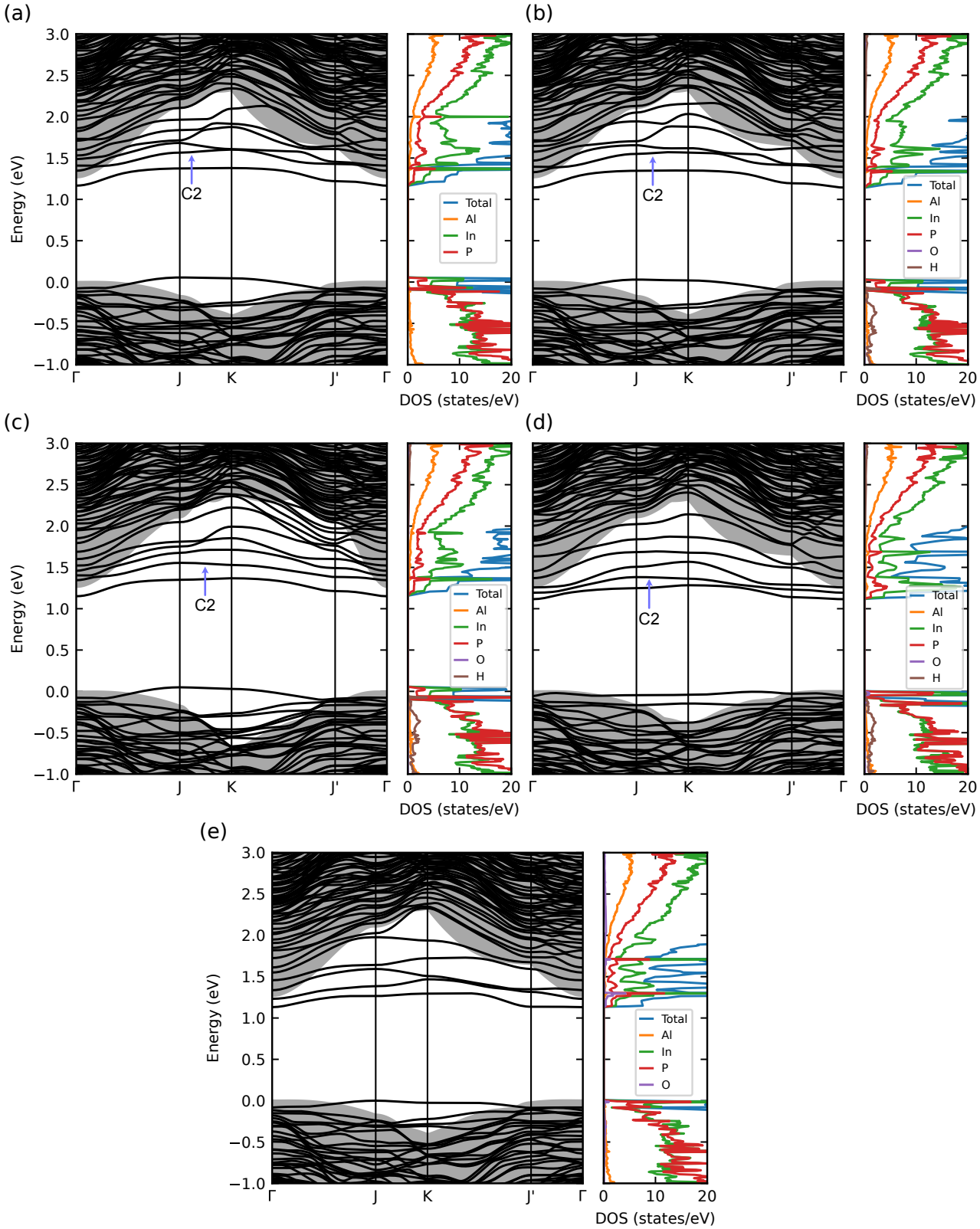

Figure S15: Band structure and the partially-decomposed density of states for the AlInP (2×4)-rInMD clean surface (a), with an H_2O molecule adsorbed at the top $In-P$ dimer (b), an H_2O molecule adsorbed at the three-fold coordinated In atom of the second row (c), an OH and H adsorbed (d) and an O atom adsorbed (e). The shaded areas indicate the projected bulk band structure. The adsorbed geometries are explained in the main text.

Table S5: Peak maximum position of core levels and VBM before and after 20 kL H_2O exposure and following O_2 exposure (2 days at 1 atm.

Core levels	Peak maximum position (eV)					
	as-prepared In-rich		after 20 kL H_2O		after O_2	
	90°	15°	90°	15°	90°	15°
Al 2p	74.18	73.94	74.50	74.38	74.50	74.37
P 2p	129.00	128.75	129.34	129.22	129.36	129.24
In $3d_{5/2}$	444.70	444.52	445.05	445.03	445.07	445.10
O 1s	—	—	532.01	532.06	532.16	532.29

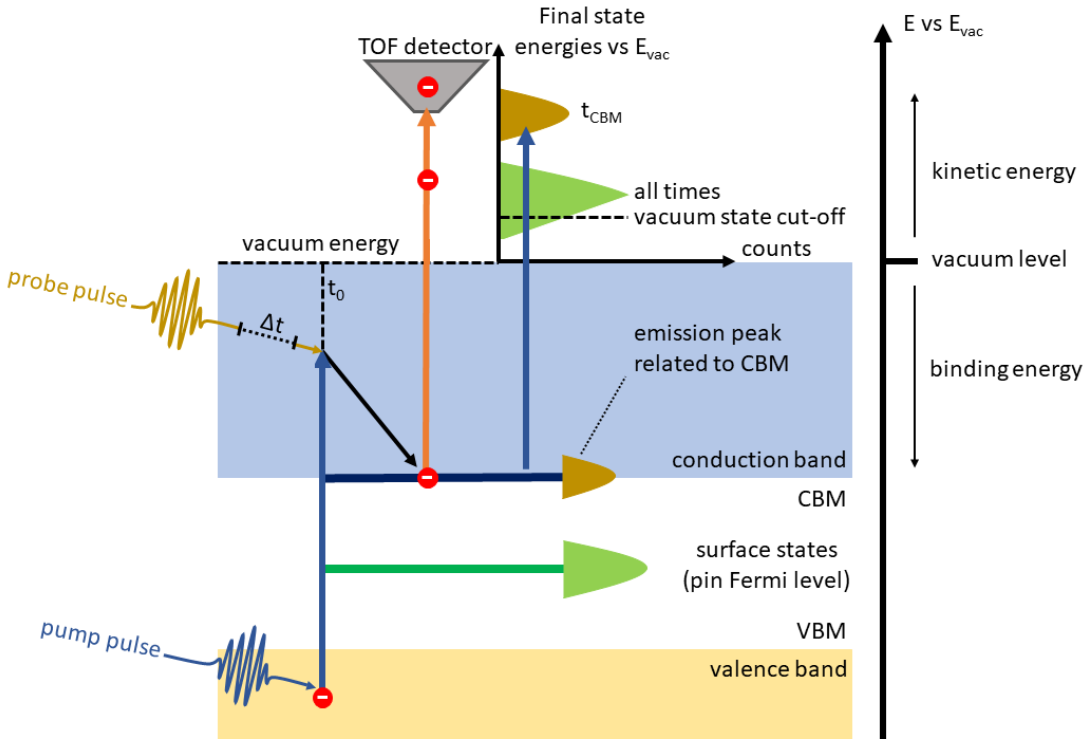

Figure S16: Schematic showing the excitation and emission pathways for tr-2PPE. Electrons are photoexcited from occupied states in the valence band, or surface states in the band gap by a pump pulse at t = 0. Photoexcited electrons the thermalize through conduction band states, from where they are photoemitted by a probe pulse after a variable time delay. By scanning over time delay and recording the kinetic energies of electrons in a TOF detector, electron relaxation paths and electronic band structure in the near-surface region are obtained. Reproduction under terms of the CC-BY 4.0 license. [38], 2024, published by American Chemical Society.

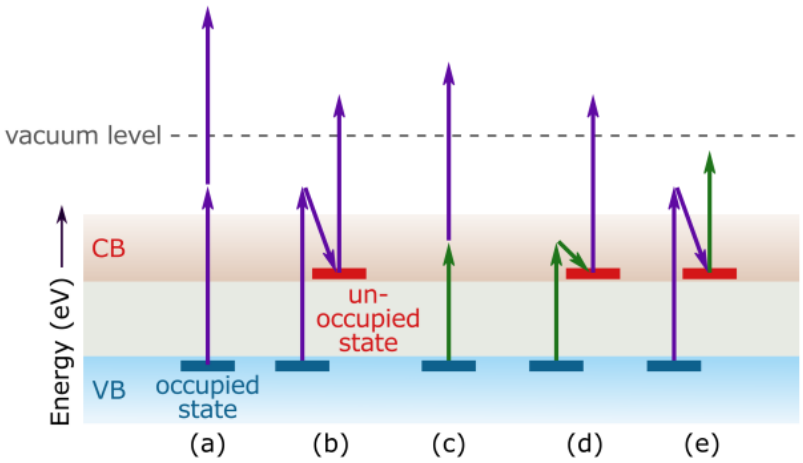

Figure S17: Schematic of two-photon photoemission using two different frequencies as pump or probe (to scale for 276 nm UV and 533 nm VIS) Reproduced under terms of the CC-BY 4.0 license. [38], 2024, published by American Chemical Society. In (a), two UV photons are incident simultaneously, in (b) a UV photon photoexcites an electron, which decays down to the next-lowest state and is emitted from there by a second UV photon. (c) and (d) show a combination of two different photon energies. In (c), a VIS photon pumps an electron which is emitted by a UV photon. In (e) an electron is pumped by the UV photon, but then thermalizes too much energy before incidence of the VIS photon, and no emission of electrons is observed.

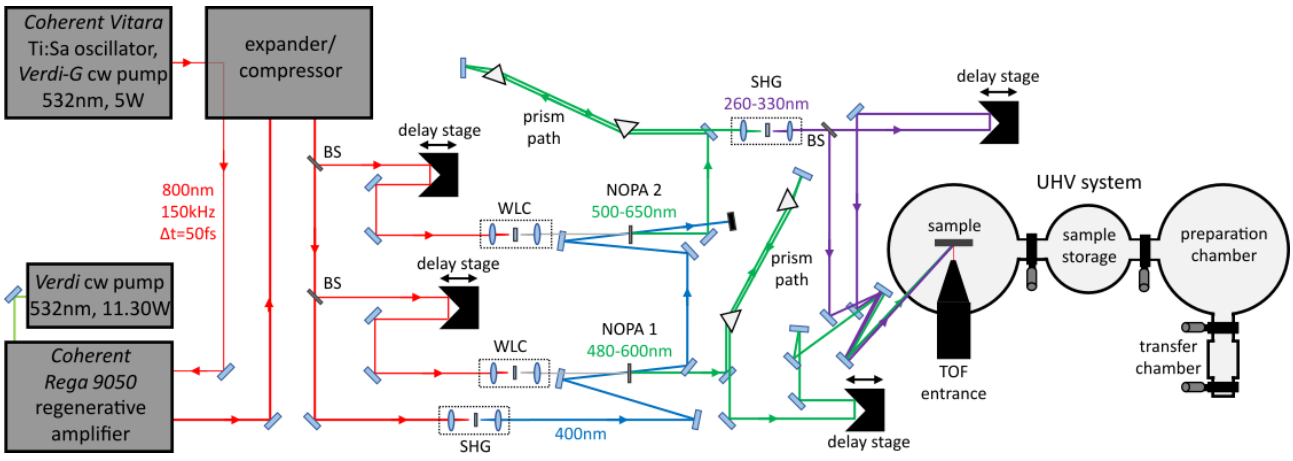

Figure S18: Schematic of the overall tr-2PPE set-up, simplified to enhance presentation, Reproduced under terms of the CC-BY 4.0 license. [38], 2024, published by American Chemical Society. The pulse-generating and -amplifying elements are on the left, NOPA 1 and 2 including 800 nm to 400 nm SHG in the middle. A prism path after each NOPA is shown, the output of NOPA 1 serves as the VIS pump, the output of NOPA 2 is frequency doubled in SHG and split to generate the UV pump and probe beams. All three beams are co-incident on the sample, which is placed in the UHV system, with the TOF detector placed 3-5 mm from the sample.

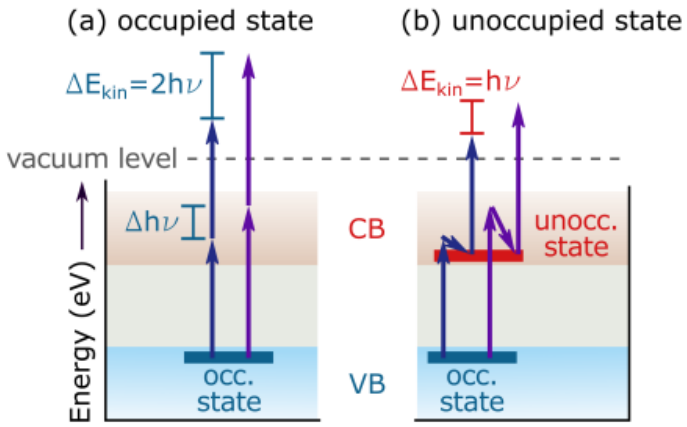

Figure S19: Tr-2PPE pathways are shown for an occupied VB state (a), and for an unoccupied CB state (b). Reproduced under terms of the CC-BY 4.0 license. [38], 2024, published by American Chemical Society.

References

[1] D. C. Moritz, I. A. Ruiz Alvarado, M. A. Zare Pour, A. Paszuk, T. Frieß, E. Runge, J. P. Hofmann, T. Hannappel, W. G. Schmidt, and W. Jaegermann. "P-terminated InP (001) surfaces: surface band bending and reactivity to water". In: *ACS Appl. Mater. Interfaces* 14 (41 2022), pp. 47255–47261. ISSN: 19448252. DOI: 10.1021/acsami.2c13352.

[2] A. Hajduk, M. V. Lebedev, B. Kaiser, and W. Jaegermann. "Interaction of liquid water with the p-$GaInP_2$(100) surface covered with submonolayer oxide". In: *Phys. Chem. Chem. Phys.* 20 (32 2018), pp. 21144–21150. ISSN: 14639076. DOI: 10.1039/c8cp03337d.

[3] M. V. Lebedev, G. M. Savchenko, N. S. Averkiev, A. Hajduk, B. Kaiser, and W. Jägermann. "Surface potential in n- and p-$GaInP_2$(100): temperature effect". In: *J. Phys. D: Appl. Phys.* 54.18 (2021), p. 185104. DOI: 10.1088/1361-6463/abe270.

[4] A. Hajduk, M. A. Zare Pour, A. Paszuk, M. Guidat, M. Löw, F. Ullmann, D. C. Moritz, J. P. Hofmann, S. Krischok, E. Runge, W. G. Schmidt, W. Jaegermann, M. M. May, and T. Hannappel. Ed. by Klaus Wandelt and Gianlorenzo Bussetti. Oxford, UK: Elsevier, 2024, pp. 120–156. ISBN: 978-0-323-85670-6. DOI: 10.1016/B978-0-323-85669-0.00113-6.

[5] M. Faur, D. T. Jayne, M. Goradia, and C. Goradia. "XPS investigation of anodic oxides grown on p-type InP". In: *Surf. Interface Anal.* 15.11 (1990), pp. 641–650.

[6] S. Ge, B. Wang, J. Lin, and L. Zhang. "C,N-Codoped InOOH Microspheres: One-Pot Synthesis, Growth Mechanism and Visible Light Photocatalysis". In: *CrystEngComm* 15.4 (2013), pp. 721–728. DOI: 10.1039/C2CE26373D.

[7] Z. Li, Z. Xie, Y. Zhang, L. Wu, X. Wang, and X. Fu. "Wide Band Gap p-Block Metal Oxyhydroxide InOOH: A New Durable Photocatalyst for Benzene Degradation". In: *J. Phys. Chem. C* 111.49 (2007), pp. 18348–18352. DOI: 10.1021/jp076107r.

[8] J. A. Taylor. "An XPS study of the oxidation of AlAs thin films grown by MBE". In: *J. Vac. Sci. Technol.* 20.3 (1982), pp. 751–755. DOI: 10.1116/1.571450.

[9] S.-L. Chang, J. W. Anderegg, and P. A. Thiel. "Surface oxidation of an Al–Pd–Mn quasicrystal, characterized by X-ray photoelectron spectroscopy". In: *J. Non-Cryst. Solids* 195.1–2 (1996), pp. 95–101. DOI: 10.1016/0022-3093(95)00537-4.

[10] E. O. Filatova and A. S. Konashuk. "Interpretation of the Changing the Band Gap of Al_2O_3 Depending on Its Crystalline Form: Connection with Different Local Symmetries". In: *J. Phys. Chem. C* 119.35 (2015), pp. 20755–20761. DOI: 10.1021/acs.jpcc.5b06843.

[11] I. Costina and R. Franchy. "Band gap of amorphous and well-ordered Al_2O_3 on Ni_3Al(100)". In: *Appl. Phys. Lett.* 78.26 (2001), pp. 4139–4141. DOI: 10.1063/1.1380403.

[12] F. Rueda, J. Mendialdua, A. Rodriguez, R. Casanova, Y. Barbaux, L. Gengembre, and L. Jalowiecki. "Characterization of Venezuelan laterites by X-ray photoelectron spectroscopy". In: *J. Electron Spectrosc. Relat. Phenom.* 82.3 (1996), pp. 135–143. DOI: 10.1016/S0368-2048(96)03035-6.

[13] D. Kim, J. H. Jung, and J. Ihm. "Theoretical Study of Aluminum Hydroxide as a Hydrogen-Bonded Layered Material". In: *Nanomaterials* 8.6 (2018), p. 375. DOI: 10.3390/nano8060375.

[14] H. He, K. Alberti, T. L. Barr, and J. Klinowski. "ESCA Studies of Aluminophosphate Molecular Sieves". In: *J. Phys. Chem.* 97.51 (1993), pp. 13703–13707. DOI: 10.1021/j100153a045.

[15] H. J. Levinson, F. Greuter, and E. W. Plummer. "Experimental Band Structure of Aluminum". In: *Phys. Rev. B* 27 (1983), pp. 727–738. DOI: 10.1103/PhysRevB.27.727.

[16] A. Alemi, Z. Hosseinpour, M. Dolatyari, and A. Bakhtiari. "Boehmite (γ-AlOOH) Nanoparticles: Hydrothermal Synthesis, Characterization, pH-Controlled Morphologies, Optical Properties, and DFT Calculations". In: *Phys. Status Solidi B* 249.6 (2012), pp. 1264–1270. DOI: 10.1002/pssb.201147484.

[17] X. Zhou, J. Zhang, Y. Ma, H. Tian, Y. Wang, Y. Li, L. Jiang, and Q. Cui. "The Solvothermal Synthesis of γ-AlOOH Nanoflakes and Their Compression Behaviors Under High Pressures". In: *RSC Adv.* 7.9 (2017), pp. 4904–4911. DOI: 10.1039/C6RA27571K.

[18] D. T. Clark, T. Fok, G. G. Roberts, and R. W. Sykes. "An investigation by electron spectroscopy for chemical analysis of chemical treatments of the (100) surface of n-type InP epitaxial layers for Langmuir film deposition". In: *Thin Solid Films* 70.2 (1980), pp. 261–283. DOI: 10.1016/0040-6090(80)90367-3.

[19] T. Lindblad, B. Rebenstorf, Z.-G. Yan, and S. L. T. Andersson. "Characterization of vanadia supported on amorphous $AlPO_4$ and its properties for oxidative dehydrogenation of propane". In: *Appl. Catal., A* 112.2 (1994), pp. 187–208. ISSN: 0926-860X. DOI: 10.1016/0926-860X(94)80219-X.

[20] Y. Muraoka and K. Kihara. "The temperature dependence of the crystal structure of berlinite, a quartz-type form of $AlPO_4$". In: *Phys. Chem. Miner.* 24 (1997), pp. 243–253. DOI: 10.1007/s002690050036.

[21] T. Barr, J. Klinowski, H. He, and K. Alberti. "Evidence for strong acidity of the molecular sieve cloverite". In: *Nature* 365 (1993), pp. 429–431. DOI: 10.1038/365429a0.

[22] T. D. Kühne, M. Iannuzzi, M. Del Ben, V. V. Rybkin, P. Seewald, F. Stein, T. Laino, R. Z. Khaliullin, O. Schütt, F. Schiffmann, D. Golze, J. Wilhelm, S. Chulkov, M. H. Bani-Hashemian, V. Weber, U. Borštnik, M. Taillefumier, A. S. Jakobovits, A. Lazzaro, H. Pabst, T. Müller, R. Schade, M. Guidon, S. Andermatt, N. Holmberg, G. K. Schenter, A. Hehn, A. Bussy, F. Belleflamme, G. Tabacchi, A. Glöß, M. Lass, I. Bethune, C. J. Mundy, C. Plessl, M. Watkins, J. VandeVondele, M. Krack, and J. Hutter. "CP2K: An electronic structure and molecular dynamics software package - Quickstep: Efficient and accurate electronic structure calculations". In: *J. Chem. Phys.* 152.19 (2020), p. 194103. ISSN: 0021-9606. DOI: 10.1063/5.0007045.

[23] J. VandeVondele, M. Krack, F. Mohamed, M. Parrinello, T. Chassaing, and J. Hutter. "QUICKSTEP: Fast and accurate density functional calculations using a mixed Gaussian and plane waves approach". In: *Comput. Phys. Commun.* 167 (2005), pp. 103–128. DOI: 10.1016/j.cpc.2004.12.014.

[24] J. VandeVondele and J. Hutter. "An efficient orbital transformation method for electronic structure calculations". In: *J. Chem. Phys.* 118 (2003), pp. 4365–4369. DOI: 10.1063/1.1564019.

[25] J. P. Perdew, K. Burke, and M. Ernzerhof. "Generalized gradient approximation made simple". In: *Phys. Rev. Lett.* 77 (18 1996), pp. 3865–3868. ISSN: 10797114. DOI: 10.1103/PhysRevLett.77.3865.

[26] J. P. Perdew, K. Burke, and Y. Wang. "Generalized gradient approximation for the exchange-correlation hole of a many-electron system". In: *Phys. Rev. B* 54.23 (1996), p. 16533. DOI: 10.1103/PhysRevB.54.16533.

[27] J. VandeVondele and J. Hutter. "Gaussian basis sets for accurate calculations on molecular systems in gas and condensed phases". In: *J. Chem. Phys.* 127 (2007), p. 114105. DOI: 10.1063/1.2770708.

[28] C. Hartwigsen, S. Goedecker, and J. Hutter. "Relativistic Separable Dual-Space Gaussian Pseudopotentials from H to Rn". In: *Phys. Rev. B* 58 (1998), pp. 3641–3662. DOI: 10.1103/PhysRevB.58.3641.

[29] M. Krack. "Pseudopotentials for H to Kr Optimized for Gradient-Corrected Exchange-Correlation Functionals". In: *Theor. Chem. Acc.* 114 (2005), pp. 145–152. DOI: 10.1007/s00214-005-0655-y.

[30] S. Grimme, J. Antony, S. Ehrlich, and H. Krieg. "A Consistent and Accurate Ab Initio Parametrization of Density Functional Dispersion Correction (DFT-D) for the 94 Elements H-Pu". In: *J. Chem. Phys.* 132 (2010), p. 154104. DOI: 10.1063/1.3382344.

[31] S. Nose. "A Unified Formulation of the Constant Temperature Molecular Dynamics Methods". In: *J. Chem. Phys.* 81 (1984), pp. 511–519. DOI: 10.1063/1.447334.

[32] G. J. Martyna, M. L. Klein, and M. Tuckerman. "Nose-Hoover chains: The Canonical Ensemble via Continuous Dynamics". In: *J. Chem. Phys.* 97 (1992), pp. 2635–2643. DOI: 10.1063/1.463940.

[33] S. Nose. "A Molecular Dynamics Method for Simulations in the Canonical Ensemble". In: *Mol. Phys.* 52 (1970), pp. 255–268. DOI: 10.1080/00268978400101201.

[34] D. Asthagiri, Lawrence R. Pratt, and J. D. Kress. "Free energy of liquid water on the basis of quasichemical theory and ab initio molecular dynamics". In: *Phys. Rev. E* 68 (4 2003), p. 041505. DOI: 10.1103/PhysRevE.68.041505.

[35] M. A. Zare Pour, S. Shekarabi, I. A. Ruiz Alvarado, J. Diederich, Y. Gao, A. Paszuk, D. C. Moritz, W. Jägermann, D. Friedrich, R. van de Krol, W. G. Schmidt, and T. Hannappel. "Exploring Electronic States and Ultrafast Electron Dynamics in AlInP Window Layers: The Role of Surface Reconstruction". In: *Adv. Funct. Mater.* n/a.n/a (2025), p. 2423702. DOI: 10.1002/adfm.202423702.

[36] Y. A Goldberg and N. M. Schmidt. "Handbook series on semiconductor parameters". In: *Vol* 2 (1999), pp. 1–36.

[37] M. Vaisman, K. Mukherjee, T. Masuda, K. N. Yaung, E. A. Fitzgerald, and M. L. Lee. "Direct-gap 2.1–2.2 eV AlInP solar cells on GaInAs/GaAs metamorphic buffers". In: *2015 IEEE 42nd PVSC*. Portland, OR, USA, December, 2015. DOI: 10.1109/PVSC.2015.7356435.

[38] J. Diederich, J. V. Rojas, M. A. Zare Pour, I. A. Ruiz Alvarado, A. Paszuk, R. Sciotto, C. Höhn, K. Schwarzburg, D. Ostheimer, R. Eichberger, W. G. Schmidt, T. Hannappel, R. van de Krol, and D. Friedrich. "Unraveling electron dynamics in p-type indium phosphide (100): A time-resolved two-photon photoemission study". In: *J. Am. Chem. Soc.* 146 (13 2024), pp. 8949–8960. ISSN: 15205126. DOI: 10.1021/jacs.3c12487.